nature electronics

ARTICLES

https://doi.org/10.1038/s41928-021-00542-8

Check for updates

A spin–orbit torque device for sensing three-dimensional magnetic fields

Ruofan Li[1,5], Shuai Zhang[1,5], Shijiang Luo[1], Zhe Guo[1], Yan Xu[2], Jun Ouyang[1], Min Song[3], Qiming Zou[4], Li Xi[2], Xiaofei Yang[1], Jeongmin Hong[1] and Long You[1] ✉

Magnetic field sensors are important in a variety of applications, including transport and medical devices. However, existing solid-state approaches for the detection of three-dimensional magnetic fields require multiple sensors, making the set-ups bulky. Here, we show that a single spin–orbit torque device composed of a Ta/CoFeB/MgO heterostructure can detect a vector magnetic field. In-plane and out-of-plane field components lead to the displacement of domain walls in the CoFeB layer, modulating the associated anomalous Hall effect resistance. Modulation of the anomalous Hall effect resistance varies linearly with the *x*, *y* and *z* components of a vector magnetic field. Our compact three-dimensional magnetic field sensor exhibits good linearity within a certain range (3.2%, 2.7% and 4.3% for the *x*, *y* and *z* directions, respectively) and high sensitivity (205, 282 and 1,845 V A^{-1} T^{-1} for the *x*, *y* and *z* directions, respectively). The sensor also exhibits low 1/*f* noise.

The precise measurement of magnetic fields is required in a range of fields, including space[1], navigation and mechanical systems[2], the automotive industry[3], biomedicine[4] and industrial automation[5]. In recent years, various types of magnetometer have been developed, such as superconducting quantum interference devices[6,7], fluxgate sensors[8] and graphene Hall sensors[9]. Approaches based on optical nitrogen vacancies in diamond[10–15], the Hall effect in semiconductor materials[16] and the spin-dependent resistance effect in magnetic materials[17,18] have also been developed. Of particular interest, sensors based on spin-dependent magnetoresistance effects—anisotropy magnetoresistance (AMR)[19], giant magnetoresistance (GMR)[20] and tunnelling magnetoresistance (TMR)[21,22]—have the advantages of wide bandwidth, high stability, small size and low cost, as well as excellent sensitivity, resolution and linearity[23].

A range of techniques have been developed that can measure a three-dimensional (3D) magnetic field[24–28]. One conventional method is to use three magnetic sensors with their sensing directions along the three coordinate axes (*x*, *y* and *z*)[25,28] or planar sensors with an attached magnetic flux guide[29,30]. However, all of these approaches are limited by the experimental set-up and environmental effects, which lead to non-orthogonality of the three sensing directions. This can result in complicated adjustments of the subunits, low signal levels, high cross-sensitivities, numerous electrical connections and the three magnetic field components not being measured at the same spot.

In this Article, we report a 3D magnetic field sensor based on a single spin–orbit torque (SOT) device composed of a Ta/CoFeB/MgO heterostructure. In our device, a 3D magnetic field, in combination with an in-plane (IP) current bias, induces domain wall (DW) motion, which modulates the anomalous Hall effect (AHE) resistance of the CoFeB layer. We derive the relationships between the measured AHE resistance and the three orthogonal components of the vector magnetic field, and show that they are linear for certain ranges. In particular, the sensor has a linear range between −10 and +10 Oe for the magnetic field components in the *x* and *y* directions and between −4 and +4 Oe for the *z* direction, which is larger than the range of a commercial 3D magnetic sensor.

Sensing principle and experimental set-up

Figure 1a shows a schematic of our 3D magnetic field sensor with the definition of the *x*–*y*–*z* coordinates. A stack consisting of Ta(10 nm)/CoFeB(1.2 nm)/MgO(1.6 nm)/Ta is patterned into Hall bar structures by standard photolithography and ion-milling techniques. The lateral size of the device, unless otherwise noted, is 50 × 200 μm^2. Our samples have a Curie temperature of 1,086 K, a saturation magnetization (M_s) of 1,004 e.m.u. cm^{-3} and effective anisotropy (K_{eff}) of 2.26 × 10^5 J m^{-3} at room temperature (Supplementary Section 1).

As a result of the spin Hall[17] or Rashba[31] effect of Ta in the Ta/CoFeB/MgO heterostructure[32], with perpendicular magnetic anisotropy (PMA), a DW can be driven by an IP current (here, J_x or J_y) along with a collinear IP magnetic field (H_x, H_y) via SOT. Theoretically, the SOT effective field plays a role like an out-of-plane (OOP) field and can be given by[33]

$$H_z^{SOT} = \frac{\hbar}{2eM_s t}\theta_{SH} J_{x(y)} m_{x(y)} \quad (1)$$

where $\hbar$ is the reduced Planck constant, e is the electron charge, M_s is the saturation magnetization, t is the thickness of the CoFeB layer, θ_{SH} is the spin Hall angle of Ta and $J_{x(y)}$ is the current density. The IP field is utilized to orient the magnetization within the DW to achieve an IP component $m_{x(y)}$. In particular, when a small IP field is applied, a longitudinal DW can be formed in the CoFeB layer and the DW propagates in a direction orthogonal to the current direction[34] (Fig. 1b,c). Moreover, at zero magnetic field, the longitudinal DW is located at the centre of the CoFeB layer, resulting in an AHE resistance of ~0 Ω. As the magnitude of the IP field changes, the DW can move from the initial position to a new pinned position[35]. On the other hand, an OOP magnetic field (H_z) can also drive DW

[1]School of Optical and Electronic Information and Wuhan National Laboratory for Optoelectronics, Huazhong University of Science and Technology, Wuhan, China. [2]Key Laboratory for Magnetism and Magnetic Materials of Ministry of Education and School of Physical Science and Technology, Lanzhou University, Lanzhou, China. [3]Faculty of Physics and Electronic Science, Hubei University, Wuhan, China. [4]Department of Electrical and Computer Engineering, University of Nebraska–Lincoln, Lincoln, NE, USA. [5]These authors contributed equally: Ruofan Li, Shuai Zhang. ✉e-mail: lyou@hust.edu.cn

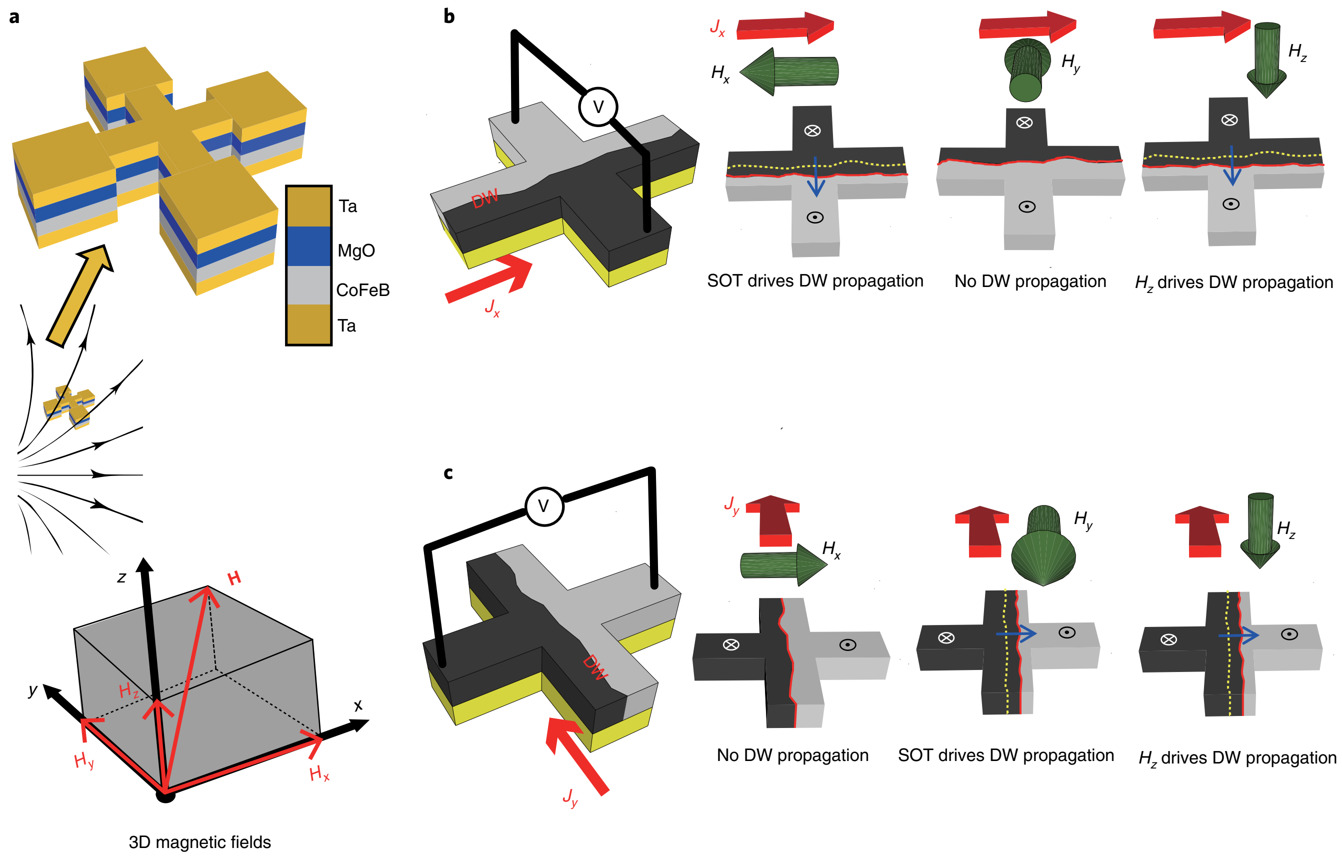

Fig. 1 | Three-dimensional magnetic field sensing based on a Ta/CoFeB/MgO heterostructure. a, Schematic of the 3D sensor placed in a vector magnetic field, and definition of the *x*–*y*–*z* coordinates. **b**, Schematics of the AHE measurement set-up and DW motion under H_x, H_y and H_z when J_x is applied. The yellow dotted line shows the initial position of the DW and the red solid line is its final position. The blue arrow indicates the direction of DW motion. **c**, Schematics of the AHE measurement set-up and DW motion under H_x, H_y and H_z when J_y is applied.

motion in the CoFeB layer, with its easy axis along the z direction. Hence, when a current is applied along the x axis, both H_x and H_z can drive DW motion, as shown in Fig. 1b. Because H_y is perpendicular to the current direction, no SOT exists and thus no DW motion occurs[36]. Similarly, if the applied current is along the y axis, H_y and H_z will contribute to DW motion, while H_x makes no contribution, as illustrated in Fig. 1c.

Furthermore, when a 3D magnetic field $\mathbf{H}=(H_x,H_y,H_z)$ and an IP current are applied to the device, the DW displacement is modulated by the combination of the IP and OOP fields. For the IP-field-driven DW motion case, the direction of H_z^{SOT} depends on both the current and IP field directions, according to equation (1). Consequently, the direction of DW motion also depends on both the current and IP field directions. Indeed, as the current direction reverses, the DW motion reverses. For the OOP-field-driven DW motion case, in contrast, the direction of DW motion is only related to the H_z direction, regardless of the current direction. These different relations between DW motion and current direction make it feasible to separate the contributions of the IP and OOP fields (as will be described below). In other words, it is possible to detect both the IP field (H_x and H_y) and OOP field (H_z) by characterizing the DW dynamics.

DW motion is accompanied by a change in the vertical component of the magnetization, M_z. To quantitatively monitor the magnetization change under different magnetic fields, AHE resistance measurements[37–39] are performed to identify the equilibrium magnetization at room temperature. While the current is applied along the x and y directions, the Hall voltage is detected in the y and x directions, and the AHE resistances R_{xy} and R_{yx} are thus recorded, respectively. Note that GMR and TMR measurements can also be used to identify the magnetization and are applicable to our 3D sensor.

One-dimensional magnetic field sensing

The AHE loop of R_{xy} versus H_z shows hysteresis with sharp switching, indicating a strong PMA of the device (black curve, inset of Fig. 2a). We investigated SOT-induced magnetization switching, as further shown in Supplementary Section 2. When a current J_x is applied, the coercive field of the AHE loop decreases as J_x increases. At $J_x=+6.8\,\mathrm{MA\,cm^{-2}}$, the hysteresis becomes close to zero (blue curve, inset of Fig. 2a). A good linear region appears in the vicinity of zero magnetic field (from −4 to +4 Oe), where R_{xy} is proportional to H_z (Fig. 2a). We also investigated the AHE loops of R_{xy} versus H_x and H_y. At $J_x=+6.8\,\mathrm{MA\,cm^{-2}}$, R_{xy} varies linearly with applied H_x within the range −10 to +10 Oe (Fig. 2b). On the other hand, the AHE loop of R_{xy} versus H_y in Fig. 2c shows that R_{xy} is maintained constant, because no DW motion occurs under H_y, as discussed above. Overall, it is seen that R_{xy} is sensitive to H_x and H_z, but insensitive to H_y, when J_x is applied. Similarly, R_{yx} is sensitive to H_y and H_z, but insensitive to H_x, when J_y is applied (Fig. 2d–f). These experimental results are consistent with the theoretical expectations described in the previous section. We also estimated the Joule heating generated by the writing current. Importantly, the device temperature under $J=6.8\,\mathrm{MA\,cm^{-2}}$ (~430 K) is much lower than the Curie temperature of our Ta/CoFeB/MgO/Ta films (~1,086 K), which agrees with a previous report[40]. At the operation temperature (~430 K), M_s and

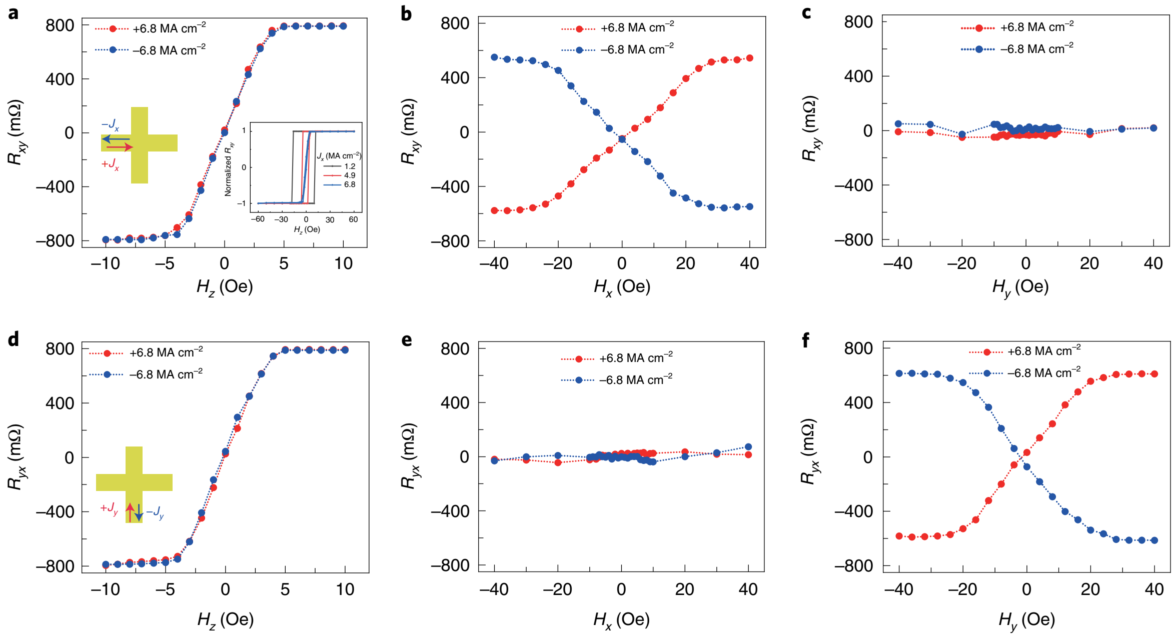

Fig. 2 | Measured *R*–*H* curves under ±6.8 MA cm−2. **a**, R_{xy} as a function of H_z. The red and blue curves represent the variation of R_{xy} with H_z under J_x = +6.8 MA cm−2 and −6.8 MA cm−2, respectively. The two curves coincide with each other. The inset shows the AHE loops under different currents. The coercive field of the AHE loop decreases as J_x increases. At J_x = +6.8 MA cm−2, the hysteresis becomes close to zero. **b**, R_{xy} as a function of H_x. The red and blue curves under +6.8 MA cm−2 and −6.8 MA cm−2, respectively, are symmetrical about the horizontal ordinate. **c**, R_{xy} as a function of H_y. R_{xy} is kept almost constant, because no DW motion occurs under H_y. **d**–**f**, R_{yx} as a function of H_z (**d**), H_x (**e**) and H_y (**f**) under J_y = +6.8 and −6.8 MA cm−2, respectively. The dotted lines are guides to the eye.

K_{eff} are estimated to be ~890 e.m.u. cm^{-3} and 1.34×10^5 J m^{-3}, respectively, indicating that the PMA just decreases rather than vanishes (Supplementary Section 1). The natural cooling process from 430 K to room temperature consumes around 40 ms (from a COMSOL simulation), which can be greatly reduced to tens of nanoseconds by introducing a thermal conducting layer and optimizing the system structure[41–43] (Supplementary Section 3).

The relationships between R_{xy} (R_{yx}) and H_x, H_y and H_z under J_x (J_y) = −6.8 MA cm^{-2} are also depicted in Fig. 2a–f (blue curves). The R_{xy}–H_z and R_{yx}–H_z curves are unchanged when the current polarity reverses. In this case, the positive H_z always favours upward magnetization ($M_z > 0$), corresponding to a positive AHE resistance ($R > 0$), while the negative H_z favours $M_z < 0$ and $R < 0$. By contrast, the R_{xy}–H_x (R_{yx}–H_y) curves under ±6.8 MA cm^{-2} are symmetrical about the horizontal ordinate. At J_x (J_y) = +6.8 MA cm^{-2}, positive H_x (H_y) favours $M_z > 0$ and increasing H_x (H_y) results in a gradual increase of R (red curve). When J_x (J_y) is reversed (−6.8 MA cm^{-2}), increasing H_x (H_y) now drives the DW towards the direction of decreasing M_z, corresponding to a gradual decrease of R (blue curve).

For further verification, we also performed magneto-optical Kerr effect (MOKE) microscopy and micromagnetic simulations to investigate the DW dynamics of the device. In the MOKE images, DW displacement is observed to scale linearly with the applied field under IP current when scanning both H_x (ranging from approximately −10 to +10 Oe) and H_z (approximately −4 to +4 Oe), consistent with the R_{xy}–H_x and R_{xy}–H_z measurement curves, respectively. In addition, results from micromagnetic simulations performed using the object-oriented micromagnetic framework (OOMMF) confirmed the experimental observations (Supplementary Section 4).

Three-dimensional magnetic field sensing

Next, we consider a 3D magnetic field $\mathbf{H} = (H_x, H_y, H_z)$ applied on the device. We can measure two AHE resistance values under positive and negative current densities in the x axis: R_{xy} ($+J_x$) and R_{xy} ($-J_x$). According to the symmetry of the R–H curves under different current polarities (Fig. 2), if the two AHE resistance values are processed with a subtraction operation, enabling elimination of the H_z contribution, the net resistance contributed by only the H_x component can be obtained as

$$R(H_x) = \frac{R_{xy}(+J_x) - R_{xy}(-J_x)}{2} \qquad (2)$$

By performing an add operation to eliminate the H_x contribution, we can obtain the net resistance contributed by only H_z as

$$R(H_z) = \frac{R_{xy}(+J_x) + R_{xy}(-J_x)}{2} \qquad (3)$$

Similarly, if we exchange the current terminals to apply J_y, the net resistance contributed by only H_y can be sensed as

$$R(H_y) = \frac{R_{yx}(+J_y) - R_{yx}(-J_y)}{2} \qquad (4)$$

Note that $R(H_z)$ can also be calculated as

$$R(H_z) = \frac{R_{yx}(+J_y) + R_{yx}(-J_y)}{2} \qquad (5)$$

and the calculation result of equation (5) is expected to be the same as that of equation (3).

The relationships between the net resistances ($R(H_x)$, $R(H_y)$, $R(H_z)$) and the corresponding magnetic field components (H_x, H_y, H_z) are calibrated based on 1D measurements. By performing a calculation between the two R_{xy}–H_x curves at J_x = +6.8 MA cm^{-2} and

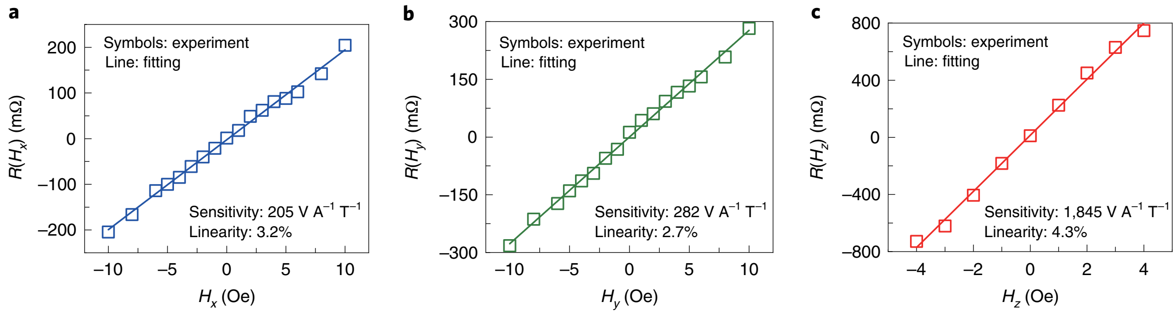

Fig. 3 | Net resistance contributed by H_x, H_y and H_z. a, Net resistance component $R(H_x)$ as a function of H_x. $R_{xy}(J_x = +6.8\,\mathrm{MA\,cm^{-2}})$ and $R_{xy}(J_x = -6.8\,\mathrm{MA\,cm^{-2}})$ under different H_x ranging from −10 Oe to +10 Oe are processed with a subtraction operation to eliminate the contribution of H_z and obtain $R(H_x)$. The blue line is a linear fit to the experimental data points. **b**, Net resistance component $R(H_y)$ as a function of H_y. Similarly, a subtraction operation is processed to obtain the net resistance component $R(H_y)$ using $R_{yx}(J_y = +6.8\,\mathrm{MA\,cm^{-2}})$ and $R_{yx}(J_y = -6.8\,\mathrm{MA\,cm^{-2}})$. The green line shows a linear fit to the experimental data points as a function of H_y in the range of −10 Oe to +10 Oe. **c**, The net resistance component $R(H_z)$ as a function of H_z is obtained by an addition operation to eliminate the contribution of H_x. The red line is a linear fit to the experimental data points.

$J_x = -6.8\,\mathrm{MA\,cm^{-2}}$ using equation (2), the relation between $R(H_x)$ and H_x is obtained as shown in Fig. 3a. The $R(H_y)$–H_y and $R(H_z)$–H_z relations are shown in Fig. 3b,c, respectively. Hence, once the net resistance components are obtained using equations (2) to (5), the corresponding magnitude of the magnetic field components can be read out according to Fig. 3a–c, implementing 3D magnetic field sensing.

Performance of our 3D magnetic field sensor

Based on the results shown in Fig. 3, our 3D magnetic field sensor has a linear range of approximately −10 to +10 Oe for both H_x and H_y, and approximately −4 to +4 Oe for H_z. The linearity of our sensor within the linear range is about 3.2%, 2.7% and 4.3% for H_x, H_y and H_z, respectively (the detailed calculation method is provided in the Methods). The sensitivity S is given by the relation $S = I\Delta R/\Delta H$. According to the results shown in Fig. 3, the sensitivities of our 3D sensor are calculated to be 205, 282 and 1,845 V A^{-1}T^{-1} for H_x, H_y and H_z, respectively. This performance can be further improved by using TMR measurements in magnetic tunnel junction (MTJ) structures. Specifically, the Ta/CoFeB/MgO heterostructure can be used as the free layer in MTJ stacks, in which a much larger resistance change of the TMR (a few kΩ) than of the AHE resistance (a few hundred mΩ, Fig. 3) can be realized[44]. Thus, a larger voltage variation ($I\Delta R$) will be obtained and thus significantly improve the sensitivity. Furthermore, we also propose a simple peripheral circuit for the sensor to implement fully automatic detection of a 3D magnetic field (Supplementary Section 5).

Figure 4 plots $\sqrt{S_v}$ as a function of the frequency at room temperature where S_v is the total noise power composed of Johnson noise, 1/f noise and background noise (details of the noise measurements are described in the Methods). The noise measurements clearly indicate a 1/f-noise-dominated regime until the total noise saturates at high frequencies with Johnson noise. The noise values at 1 Hz for 50- and 40-μm-wide devices (length of 200 μm) at writing current densities of 6.8 MA cm^{-2} and 6.2 MA cm^{-2} are around 1,450 and 150 nV Hz$^{-1/2}$, respectively. Joule heating contributing to the Hooge parameter could be the main factor influencing the 1/f noise, besides DW motion caused by the applied current together with a magnetic field (Supplementary Section 6). The required writing current, device resistance and, consequently, Joule heating can be reduced by scaling down the lateral device dimensions. Therefore, the noise at the writing current density can be remarkably suppressed by decreasing the device width or length. This is a highly desirable feature for achieving high-density integration of our proposed sensor. Moreover, note that the actual noise is caused by the pulsed writing currents used for our device, which is expected to be lower than that measured by d.c. currents. To further reduce the noise, we can take advantage of using a metal with high spin Hall angle to replace Ta as the spin current source (for example, W and CuBi alloys[45,46]). The performance of our 3D sensor is summarized in Table 1.

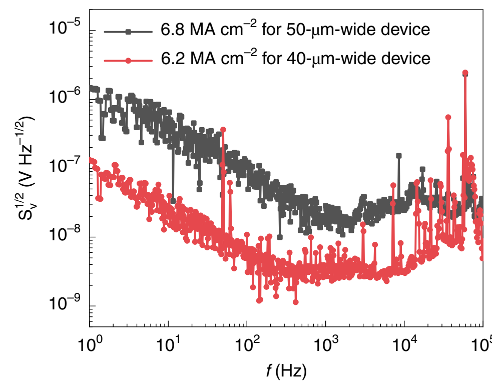

Fig. 4 | Noise spectral density. S_v is the total noise power on the y axis and f is the frequency on the x axis. The black and red curves show the noise spectral density at 6.8 MA cm^{-2} for a 50-μm-wide device and 6.2 MA cm^{-2} for a 40-μm-wide device. The 1/f noise dominates the total noise for the lower frequencies, while Johnson noise dominates at higher frequencies.

Table 1 | Performance of our 3D magnetic sensor

Characteristics	x axis	y axis	z axis	Unit
Full-scale field range (FS)	±10	±10	±4	Oe
Sensitivity	205	282	1,845	V A^{-1}T^{-1}
Linearity error within FS	3.2	2.7	4.3	%FS
1/f noise density at 1 Hz	1,450[a]			nV Hz$^{-1/2}$
	150[b]			
Resolution	7,073[a]	5,142[a]	786[a]	nT
	732[b]	532[b]	81[b]	

[a]Device dimensions: 50 μm (width) and 200 μm (length). [b]Device dimensions: 40 μm (width) and 200 μm (length).

Compared to commercial (TMR2305M, Multi-Dimension Technology) and state-of-the-art (GMR, fluxgate) 3D magnetic sensors, the linear ranges for the x and y sensing directions of our sensor (here called the SOT sensor) are ~2–6 times larger, while that for the z sensing direction is larger or comparable[47,48]. Within the detectable range, the linearity of the SOT sensor is better than that of the fluxgate magnetometer and comparable to that of the commercial TMR 3D sensor. Also, compared to the GMR and TMR 3D sensors, the noise at 1 Hz of our SOT sensor is lower, although the noise is notably lower (13.5 nV $Hz^{-1/2}$ for the x and y sensing directions and 73 nV $Hz^{-1/2}$ for the z sensing direction) in the fluxgate sensor among all the 3D sensors. We have not compared the sensitivities of the SOT sensor and GMR/TMR sensors, as they have different readout principles (AHE and MR, respectively) and thus units (V A^{-1} T^{-1} and V V^{-1} T^{-1}, respectively). Compared with a state-of-the-art AHE 1D sensor using FePt ferromagnetic films that exploits the same readout principle as our SOT sensor, the sensitivity of the SOT sensor is larger by about one order of magnitude along the x and y directions and even two orders of magnitude in the z direction[49]. It is worth noting that all other 3D sensors use three or more magnetic sensing elements that are integrated for 3D magnetic field sensing and generally suffer from cross-sensitivity among the measurement axes, seriously complicating technology fabrication, impeding high spatial resolution and obstructing achievement of the required miniaturization degree. By contrast, our SOT technology, exploiting just a single device, advantageously realizes the planarization and miniaturization of vector magnetometers (Supplementary Section 7).

Conclusions

We have reported a 3D magnetic field sensor that is based on a single SOT device with Ta/CoFeB/MgO Hall bar structure. In our device, both IP and OOP fields, under an IP current bias, can induce DW motion that modulates the AHE resistance of the device. We first derived the linear relationships between the AHE resistance and uniaxial magnetic field within a certain range. By changing the polarity of the bias current, we then derived the linear relationships between the AHE resistance and the components of the vector magnetic fields. We used our 3D sensor to probe the H_x, H_y and H_z components of the vector magnetic fields via the AHE resistance, demonstrating linearities of 3.2%, 2.7% and 4.3% and sensitivities of 205, 282 and 1,845 V A^{-1} T^{-1}, respectively. To improve the sensitivity of our sensor, MTJ structures could potentially be used. Furthermore, the 1/f noise density at low frequency can be further suppressed by using a metal with a high spin Hall angle to replace Ta as the spin Hall source, which could potentially reduce the write current.

Methods

Sample preparation. Magnetron sputtering without a post-annealing process was used to deposit a film structure of Ta(10 nm)/CoFeB(1.2 nm)/MgO(1.6 nm)/Ta(20 nm) on a thermally oxidized Si substrate at room temperature. The thin-film stack was fabricated into Hall bars by photolithography (a deep-ultraviolet lithography machine) and argon-ion milling (MIBE 150A). The top Ta was then thinned by 15 nm using argon-ion milling. To cap on pads as electrodes, magnetron sputtering was used to grow a Ta(10 nm)/Pt(100 nm) bilayer. The width and length of the channel in the Hall devices were 50 and 200 μm, respectively, and the dimensions of the device pads were 100 μm × 100 μm.

Electrical measurements. For the anomalous Hall resistance measurements, we used a d.c. current source (Keithley model 6221) to apply currents and a nanovoltmeter (Keithley model 2182A) to measure the Hall voltage. A write current ($J = \pm 6.8$ MA cm^{-2}) with a duration of 0.5 s was used for the DW motion observations mentioned in the main text. A constant reading current of 0.1 mA (~0.012 MA cm^{-2}) was applied to read out the AHE resistance.

Linearity calculation. Within the linear range of ±10 Oe for H_x and H_y and ±4 Oe for H_z, linear fitting of the data points according to a least-squares method was performed. The linearity is given by the formula $\delta = \Delta Y_{max}/Y \times 100\%$, where ΔY_{max} is the maximum deviation between the sensor experimental data and the fitted line and Y is the full-scale output.

Measurement of the noise. To perform noise measurements, we used an E5052B signal source analyzer (Keysight) to filter out the d.c. voltage signal and then output the noise signal, which varies with frequency. The writing currents were applied by a Keithley 6221 source and all tests were performed at room temperature without an external magnetic field. During each measurement for different current densities, we applied the current all the time until the noise spectrum was scanned.

MOKE imaging. MOKE images were used to magnetically image the DW motion in the CoFeB layer. We first saturated the magnet in the $-z$ or $+z$ direction, then an image was taken to serve as the reference image. The external magnetic field was then changed and, after applying a writing current for 0.5 s, another image was taken. The first reference image was subtracted from the second image to generate the final MOKE image.

Micromagnetic simulation. The DW motion was simulated by solving the Landau–Lifshitz–Gilbert (LLG) equation:

$$\frac{d\mathbf{m}}{dt} = -\gamma \mathbf{m} \times \mathbf{H}_{\mathrm{eff}} + \frac{\alpha}{M_s}\mathbf{m} \times \frac{d\mathbf{m}}{dt} + \frac{\theta_{SH} J \mu_B}{e M_s t}\mathbf{m} \times \mathbf{m} \times \mathbf{z}$$

through OOMMF, where $\mathbf{m}$ is the normalized magnetization vector for the CoFeB layer, γ is the gyro-magnetic ratio, α is the Gilbert damping constant, M_s is the saturation magnetization, J is the current density, θ_{SH} is the spin Hall angle of the heavy metal, μ_B is the Bohr magnetron, e is the elementary charge and t is the thickness of the CoFeB layer.

The effective magnetic field, $\mathbf{H}_{\mathrm{eff}}$, including the effects of uniaxial anisotropy, exchange coupling, demagnetization, the Dzyaloshinskii–Moriya interaction (DMI) and Zeeman fields, is expressed as

$$\mathbf{H}_{\mathrm{eff}} = \frac{K_u}{M_s}\mathbf{z} + \frac{2A_{ex}}{M_s^2}\nabla^2\mathbf{m} - 4\pi M_s D_{zz}\mathbf{z} + \frac{2D}{\mu_0 M_s}[(\nabla\cdot\mathbf{m})\mathbf{z} - \nabla m_z] + \mathbf{H}_{\mathrm{ext}}$$

where A_{ex} is the exchange correlation constant, K_u is the perpendicular magnetic anisotropy, D_{zz} is the demagnetization coefficient along the easy (z) axis, D is the DMI constant and $\mathbf{H}_{\mathrm{ext}}$ is the applied magnetic field. A 1,200-nm-long, 600-nm-wide and 0.6-nm-thick magnet with a mesh size of 5 nm × 5 nm × 0.6 nm was used for simulations. Material parameters used in the simulation correspond to the CoFeB thin film in the experiment, where $M_s = 1{,}100$ kA m^{-1} (measured for our materials stack by performing vibrating sample magnetometry), $A_{ex} = 3 \times 10^{-11}$ J m^{-1}, $K_u = 0.97 \times 10^6$ J m^{-3}, $\theta_{SH} = 0.1$ and $J = 1 \times 10^7$ A cm^{-2}. The micromagnetic simulator OOMMF used in this work is publicly accessible at http://math.nist.gov/oommf.

Data availability

Source data are provided with this paper. Any additional data are available from the corresponding author upon reasonable request.

Received: 13 October 2019; Accepted: 18 January 2021;
Published online: 15 February 2021

References

1. Michelena, M. D. Small magnetic sensors for space applications. *Sensors (Basel)* **9**, 2271–2288 (2009).
2. Bird, J. & Arden, D. Indoor navigation with foot-mounted strapdown inertial navigation and magnetic sensors. *IEEE Wirel. Commun.* **18**, 28–35 (2011).
3. Luo, Z. Y., Xu, Y. J., Yang, Y. M. & Wu, Y. H. Magnetic angular position sensor enabled by spin–orbit torque. *Appl. Phys. Lett.* **112**, 262405 (2018).
4. Lee, J. R. et al. Experimental and theoretical investigation of the precise transduction mechanism in giant magnetoresistive biosensors. *Sci. Rep.* **6**, 18692 (2016).
5. Reininger, T., Welker, F. & von Zeppelin, M. Sensors in position control applications for industrial automation. *Sens. Actuat. A Phys.* **129**, 270–274 (2006).
6. Shibata, Y. et al. Imaging of current density distributions with a Nb weak-link scanning nano-SQUID microscope. *Sci. Rep.* **5**, 15097 (2015).
7. Huber, M. E. et al. Gradiometric micro-SQUID susceptometer for scanning measurements of mesoscopic samples. *Rev. Sci. Instrum.* **79**, 053704 (2008).
8. Ripka, P. New directions in fluxgate sensors. *J. Magn. Magn. Mater.* **215–216**, 735–739 (2000).
9. Zheng, Y. H. et al. Sensitivity enhancement of graphene hall sensors modified by single-molecule magnets at room temperature. *RSC Adv.* **7**, 1776–1781 (2017).
10. Labanowski, D. et al. Voltage-driven, local, and efficient excitation of nitrogen-vacancy centers in diamond. *Sci. Adv.* **4**, eaat6574 (2018).
11. Wang, P. F. et al. High-resolution vector microwave magnetometry based on solid-state spins in diamond. *Nat. Commun.* **6**, 6631 (2015).
12. Maze, J. R. et al. Nanoscale magnetic sensing with an individual electronic spin in diamond. *Nature* **455**, 644–647 (2008).
13. Balasubramanian, G. et al. Nanoscale imaging magnetometry with diamond spins under ambient conditions. *Nature* **455**, 648–651 (2008).

14. Taylor, J. M. et al. High-sensitivity diamond magnetometer with nanoscale resolution. *Nat. Phys.* **4**, 810–816 (2008).
15. Zhao, N., Hu, J. L., Ho, S. W., Jones, T. K. W. & Liu, R. B. Atomic-scale magnetometry of distant nuclear spin clusters via nitrogen-vacancy spin in diamond. *Nat. Nanotechnol.* **6**, 242–246 (2011).
16. Zieren V. A new silicon micro-transducer for the measurement of the magnitude and direction of a magnetic-field vector. *Proc. International Electron Devices Meeting* 669–672 (IEEE, 1980).
17. Hirsch, J. E. Spin Hall effect. *Phys. Rev. Lett.* **83**, 1834–1837 (1999).
18. Nakayama, H. et al. Spin Hall magnetoresistance induced by a nonequilibrium proximity effect. *Phys. Rev. Lett.* **110**, 206601 (2013).
19. Dietmayer, K. C. J. *Magnetische Sensoren auf Basis des AMR-Effekts. Tech. Mess.* **68**, 269 (2009).
20. Yan, S. H. et al. Design and fabrication of full Wheatstone-bridge-based angular GMR. *Sensors (Basel)* **18**, 1832 (2018).
21. Li, P. S. et al. Electric field manipulation of magnetization rotation and tunneling magnetoresistance of magnetic tunnel junctions at room temperature. *Adv. Mater.* **26**, 4320–4325 (2014).
22. Yuasa, S., Nagahama, T., Fukushima, A., Suzuki, Y. & Ando, K. Giant room-temperature magnetoresistance in single-crystal Fe/MgO/Fe magnetic tunnel junctions. *Nat. Mater.* **3**, 868–871 (2004).
23. Ohno, H., Stiles, M. D. & Dieny, B. Spintronics. *Proc. IEEE* **104**, 1782–1786 (2016).
24. Kordic, S. Integrated 3-D magnetic sensor based on an n-p-n transistor. *IEEE Electron Device Lett.* **7**, 196–198 (1986).
25. Popovic, R. S. The vertical Hall-effect device. *IEEE Electron Device Lett.* **5**, 357–358 (1984).
26. Kordic, S. Sensitivity of the silicon high-resolution 3-dimensional magnetic-field vector sensor. *Proc. International Electron Devices Meeting* 188–191 (IEEE, 1986).
27. Wei, F. F. et al. Magnetic field sensor based on a combination of a microfiber coupler covered with magnetic fluid and a sagnac loop. *Sci. Rep.* **7**, 4725 (2017).
28. Ettelt, D. et al. 3D magnetic field sensor concept for use in inertial measurement units (IMUs). *J. Microelectromech. Syst.* **23**, 324–333 (2014).
29. Luong, V. S. et al. Planarization, fabrication and characterization of three-dimensional magnetic field sensors. *IEEE Trans. Nanotechnol.* **17**, 11–25 (2017).
30. Chen, J., Wurz, M. C., Belski, A. & Rissing, L. Designs and characterizations of soft magnetic flux guides in a 3-D magnetic field sensor. *IEEE Trans. Magn.* **48**, 1481–1484 (2012).
31. Mihai Miron, I. et al. Current-driven spin torque induced by the Rashba effect in a ferromagnetic metal layer. *Nat. Mater.* **9**, 230–234 (2010).
32. Hoffmann, A. Spin Hall effects in metals. *IEEE Trans. Magn.* **49**, 5172–5193 (2013).
33. Liu, L. Q., Lee, O. J., Gudmundsen, T. J., Ralph, D. C. & Buhrman, R. A. Current-induced switching of perpendicularly magnetized magnetic layers using spin torque from the spin Hall effect. *Phys. Rev. Lett.* **109**, 096602 (2012).
34. Bhowmik, D. et al. Deterministic domain wall motion orthogonal to current flow due to spin orbit torque. *Sci. Rep.* **5**, 11823 (2015).
35. Zhang, S. et al. Spin–orbit-torque-driven multilevel switching in Ta/CoFeB/MgO structures without initialization. *Appl. Phys. Lett.* **114**, 042401 (2019).
36. Fan, W. J. et al. Asymmetric spin–orbit-torque-induced magnetization switching with a noncollinear in-plane assisting magnetic field. *Phys. Rev. Appl.* **11**, 034018 (2019).
37. Endo, M., Kanai, S., Ikeda, S., Matsukura, F. & Ohno, H. Electric-field effects on thickness dependent magnetic anisotropy of sputtered MgO/$Co_{40}Fe_{40}B_{20}$/Ta structures. *Appl. Phys. Lett.* **96**, 212503 (2010).
38. Chang Lau, Y., Sheng, P., Mitani, S., Chiba, D. & Hayashi, M. Electric field modulation of the non-linear areal magnetic anisotropy energy. *Appl. Phys. Lett.* **110**, 022405 (2017).
39. Hayashi, Y. et al. Electric-field effect on magnetic anisotropy in Pt/Co/Pd/MgO structures deposited on GaAs and Si substrates. *Appl. Phys. Express* **11**, 013003 (2018).
40. Yamanouchi, M. et al. Domain structure in CoFeB thin films with perpendicular magnetic anisotropy. *IEEE Magn. Lett.* **2**, 3000304 (2011).
41. Papusoi, C. et al. Probing fast heating in magnetic tunnel junction structures with exchange bias. *New J. Phys.* **10**, 103006 (2008).
42. Prejbeanu, I. L. et al. Thermally assisted MRAMs: ultimate scalability and logic functionalities. *J. Phys. D* **46**, 074002 (2013).
43. Song, M. et al. Low current writing perpendicular magnetic random access memory with high thermal stability. *Mater. Des.* **92**, 1046–1051 (2016).
44. Wang, M. X. et al. Current-induced magnetization switching in atom-thick tungsten engineered perpendicular magnetic tunnel junctions with large tunnel magnetoresistance. *Nat. Commun.* **9**, 671 (2018).
45. Pai, C. F. et al. Spin transfer torque devices utilizing the giant spin Hall effect of tungsten. *Appl. Phys. Lett.* **101**, 122404 (2012).
46. Niimi, Y. et al. Giant spin Hall effect induced by skew scattering from bismuth impurities inside thin film CuBi alloys. *Phys. Rev. Lett.* **109**, 156602 (2012).
47. Jeng, J. T., Chiang, C. Y., Chang, C. H. & Lu, C. C. Vector magnetometer with dual-bridge GMR sensors. *IEEE Trans. Magn.* **50**, 1–4 (2014).
48. Lu, C. C. & Huang, J. A 3-axis miniature magnetic sensor based on a planar fluxgate magnetometer with an orthogonal fluxguide. *Sensors (Basel)* **15**, 14727–14744 (2015).
49. Zhang, Y., Hao, Q. & Xiao, G. Low-frequency noise of magnetic sensors based on the anomalous Hall effect in Fe–Pt alloys. *Sensors (Basel)* **19**, 3537 (2019).

Acknowledgements

This work was supported by the National Natural Science Foundation of China (NSFC grants 62074063, 61821003, 61904051, 61904060, 51671098 and 61674062), the National Key Research and Development Program of China (grant no. 2020AAA0109000), the Research Project of Wuhan Science and Technology Bureau (grant no. 2019010701011394) and the Fundamental Research Funds for the Central Universities (HUST: 2018KFYXKJC019). We acknowledge assistance from G. Wu and L. Zhan in providing the equipment for noise measurements.

Author contributions

L.Y. conceived the ideas and designed the experiments. S.Z. fabricated the samples and implemented the experimental set-up. R.L. performed the experimental measurements and the simulations by OOMMF and COMSOL. R.L., S.Z., Z.G., J.O. and L.Y. analysed the results. Y.X. and L.X. provided the MOKE equipment and S.Z. performed the MOKE measurements. M.S., J.H., Q.Z. and X.Y. provided the theoretical support. R.L., S.Z., S.L., Z.G. and L.Y. wrote the manuscript. All authors discussed the data and contributed to the manuscript.

Competing interests

The authors declare no competing interests.

Additional information

Supplementary information The online version contains supplementary material available at https://doi.org/10.1038/s41928-021-00542-8.

Correspondence and requests for materials should be addressed to L.Y.

Peer review information *Nature Electronics* thanks Coriolan Tiusan and the other, anonymous, reviewer(s) for their contribution to the peer review of this work.

Reprints and permissions information is available at www.nature.com/reprints.

Publisher's note Springer Nature remains neutral with regard to jurisdictional claims in published maps and institutional affiliations.